

Sequencing polymers to enable solid-state lithium batteries

Received: 4 March 2023

Accepted: 15 September 2023

Published online: 16 October 2023



Shantao Han¹, Peng Wen¹, Huaijiao Wang¹, Yang Zhou¹, Yu Gu¹, Lu Zhang¹, Yang Shao-Horn²✉, Xinrong Lin³✉ & Mao Chen¹✉

Rational designs of solid polymer electrolytes with high ion conduction are critical in enabling the creation of advanced lithium batteries. However, known polymer electrolytes have much lower ionic conductivity than liquid/ceramics at room temperature, which limits their practical use in batteries. Here we show that **precise positioning of designed repeating units in alternating polymer sequences** lays the foundation for **homogenized Li⁺ distribution, non-aggregated Li⁺-anion solvation and sequence-assisted site-to-site ion migration**, facilitating the tuning of Li⁺ conductivity by up to three orders of magnitude. The assembled all-solid-state batteries facilitate reversible and dendrite-mitigated cycling against Li metal from ambient to elevated temperatures. This work demonstrates a powerful molecular engineering means to access highly ion-conductive solid-state materials for next-generation energy devices.

Increasing the energy and lifespan of lithium-ion batteries is critical in enabling intensive electrification and decarbonization in the transportation and power sectors¹. While replacing the graphite anode with Li metal can double energy density at the system level (>500 Wh kg⁻¹)^{2,3}, innovations in electrolyte usage are needed to address challenges in regard to the poor efficiency of lithium metal and to seed future technology advances⁴. Liquid electrolytes are known for issues relating to their uncontrollable Li–electrolyte parasitic reactions and dendrites, which hinder the implementation of Li metal batteries following decades of development⁵. Although ceramic electrolytes provide high conductivity at room temperature, they are fragile and suffer from poor interfacial/dimensional stability^{6–8}. We focus on solid polymer electrolytes (SPEs), which possess excellent processability and tunable interfacial compatibility^{9,10}, offering opportunities to enable all-solid-state batteries (ASSBs). Unfortunately, a long-standing challenge in regard to SPEs is their poor ion conductivity, which prohibits the ambient-temperature use of polymers^{11,12}. To date, lithium metal-based ASSB operation with SPEs has been shown only with (1) a triblock copolymer electrolyte at 60 °C (ref. 13) and (2) a perfluoropolyether-based electrolyte at 80 °C without solvent residues¹⁴.

Ion conduction in polymer electrolytes free of solvents¹⁵ hinges on the segmental motion of polymers, where ions hop statistically among polymer coordinating sites^{6,16}. Therefore, ionic conductivity (σ) is governed by the concentration of dissociated ions (c_i) and mobility of polymer chains (μ_i)^{6,9}. Many studies have focused on increasing segmental chain motion via reduction in glass transition temperature (T_g) using plasticizing additives¹⁷, changing the types of monomer¹⁸ and tailoring macromolecular architectures¹⁹. Because both Li⁺ cations and counter-anions are mobile in conventional polymer electrolytes (for example, polyethylene oxide (PEO)), low transference number (t_{Li^+}) of 0.2–0.4 and low Li⁺ conductivity (σ_{Li^+} , $\sigma_{Li^+} = \sigma \times t_{Li^+}$) can lead to severe transport-related polarization^{20,21}. To compete with liquid/ceramic electrolytes that display 10^{-2} – 10^{-3} S cm⁻¹ (ref. 22), a minimum ionic conductivity of 1.0×10^{-4} S cm⁻¹ at ambient temperature is required for SPEs¹⁶, beyond that of state-of-the-art polymer electrolytes.

Distinct from conventional polymer electrolytes, Li cations in single-ion polymer electrolytes (SIPEs) move along the polymeric backbone with immobilized polyanions (Fig. 1), which yields t_{Li^+} close to 1 (ref. 23). Owing to the regulated anions and increased σ_{Li^+} (refs. 20,21,24), it is predicted that SIPEs could reduce ionic conductivity requirement by a factor of ten²⁵. However, uncontrolled

¹State Key Laboratory of Molecular Engineering of Polymers, Department of Macromolecular Science, Fudan University, Shanghai, China. ²Department of Materials Science and Engineering, Research Laboratory of Electronics, Department of Mechanical Engineering, Massachusetts Institute of Technology, Cambridge, MA, USA. ³Division of Natural and Applied Sciences, Duke Kunshan University, Kunshan, China. ✉e-mail: shaohorn@mit.edu; xl422@duke.edu; chenmao@fudan.edu.cn

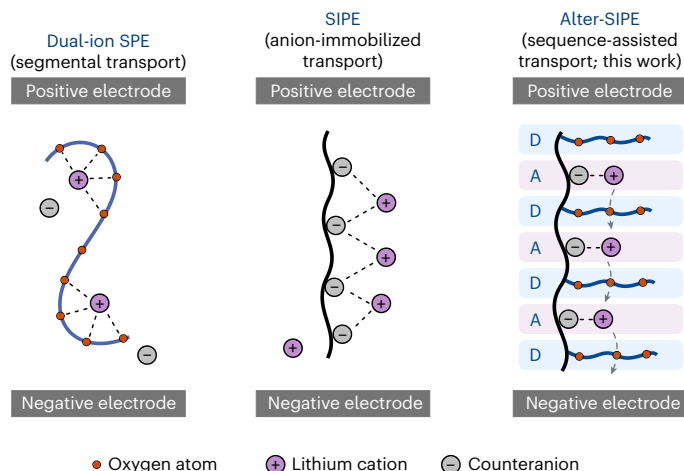


Fig. 1 | Illustration of Li^+ transport patterns during battery charging in different polymer electrolyte systems. Polymers with immobilized anions and Li^+ counterparts are designated as SIPEs. PEO electrolytes (for example, solid-state PEO-1, 20.0 kDa, and liquid-state PEO-2, 0.5 kDa, as comparative groups in this work) are typical dual-ion SPEs.

charge distribution in SIPEs forms polyanion–cation clusters that could aggravate strong ion–ion interactions between Li^+ and anionic counterparts, severely retarding Li^+ dissociation^{9,16}. The adoption of highly delocalized anionic groups such as sulfonylimides^{13,26,27} can increase dissociation compared with carbonate and sulfonate anions²³. Unfortunately, state-of-the-art SIPEs achieved σ and σ_{Li^+} only in the range 10^{-9} – $10^{-6} \text{ S cm}^{-1}$ (ref. 16), which is lower than that of conventional polymer electrolytes, necessitating leverage of new structural motifs to promote Li^+ dissociation.

Inspired by natural macromolecules that can achieve complex regulation and recognition by delicate control of not only side-chain functionalities but also sequential arrangement of monomers^{28,29}, we envision that manipulation of polymer sequence could strengthen the control of ion transport³⁰ by precise ‘encoding’ of delocalized anionic groups and regulation of ion distribution at the molecular level, promoting Li^+ dissociation in SIPEs. Herein, we report the development of a solid-state fluorinated SIPE with alternating sequence (alter-SIPE) that is composed of periodically arranged anionic and PEO pendants, creating homogeneous Li^+ distributions, non-aggregated Li^+ -anion solvation and enhanced Li^+ -anion dissociation in the SPE matrix. This microstructure leads to a concerted PEO- Li^+ -anion migration, enabling σ_{Li^+} of $\sim 4.0 \times 10^{-5} \text{ S cm}^{-1}$ at 30 °C ($t_{\text{Li}^+} = 0.93$), which is tuned up by between one and three orders of magnitude and is comparable to that of liquid-state PEO³¹. Such sequencing has lowered the operating temperature of ASSBs with dry polymer electrolytes, from 60–80 °C (refs. 13,32) to 30 °C. The fundamental importance of polymer sequence provides a new paradigm to manipulate Li^+ conduction, and informs a promising molecular strategy to access non-flammable, processable and high-performance ASSBs.

Promotion of Li^+ dissociation by sequencing

The synthesis of alter-SIPEs uses a fluorinated Li-salt monomer and PEO-substituted vinyl ethers as electronic acceptor (A) and donor (D), respectively, to ensure the cross-propagation of two monomers along the main chain in a radical reaction mechanism (Fig. 2)³³. Meanwhile, number-average molecular weight (M_n) and molecular weight distribution (D) are known to change the fundamental properties of polymers³⁴. We therefore developed a photo-controlled radical alternating copolymerization (photo-CRAP)³⁵ to yield target polymers of predefined chain length. Reactivity ratios, where each represents the relative reactivity of a radical to self-propagation with its own monomer ($k_{\text{AA}}, k_{\text{BB}}$) compared

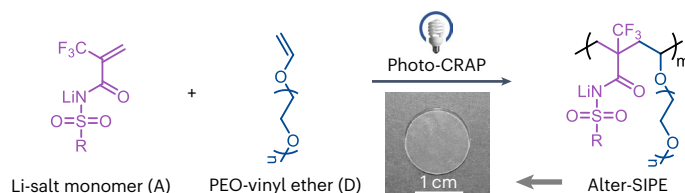


Fig. 2 | Synthesis of alter-SIPE. Photo-CRAP of electronic acceptor (A) and donor (D) monomers; inset shows the photograph of alter-SIPE.

with the other monomer ($k_{\text{AB}}, k_{\text{BA}}, r_{\text{A}} = k_{\text{AA}}/k_{\text{AB}}, r_{\text{B}} = k_{\text{BB}}/k_{\text{BA}}$), are usually used to determine polymer sequence. Following kinetic investigations (Supplementary Table 1), the reactivity ratios of both Li-salt (r_{A}) and PEO-substituted (r_{B}) vinyl compounds were found to be close to zero because $k_{\text{AA}} \ll k_{\text{AB}}$ and $k_{\text{BB}} \ll k_{\text{BA}}$ (Supplementary Fig. 1), suggesting a strong cross-propagation tendency to yield alternating sequences. To probe the effect of sequence regulation, we synthesized SIPEs of homo-, block- and random sequences for parallel comparison (Fig. 3a and Supplementary Table 2).

Molecular dynamics (MD) simulation shows that sequencing of fluorinated Li-salt monomer and PEO-substituted vinyl ether promotes ion dissociation, with alter-SIPE exhibiting maximally homogeneous Li^+ distribution among all sequences examined (Fig. 3b and Supplementary Fig. 3). According to Manning counterion condensation theory, ion dissociation in SIPE would be enhanced with increased spacing distance (L) between adjacent anionic units on the polymer backbone (Supplementary equation (5)), where reduced density of Li^+ and anions on the alternating backbone (Supplementary Table 4) is expected to provide a greater degree of Li^+ dissociation than homo-SIPE³⁶. While alter-, random- and block-SIPEs exhibit similar Li^+ densities, the lower coefficients of s.d. from the average Li^+ density in alter-SIPE (± 19.1 versus ± 26.7 and $\pm 33.7\%$; Fig. 3c) indicate greater Li^+ homogeneity and minimization of localized Li^+ ions. Uniform Li^+ distribution can facilitate dissociation and reduce cationic aggregates¹⁶. However, homo-SIPE exhibits a higher Li^+ density than SIPEs with other sequences, ascribed to the absence of PEO-based spacers that result in higher averaged ion density. The microscopic distribution of Li^+ was evaluated quantitatively by simulation of the probable r distance between two Li^+ ions using radial distribution function (RDF). In Fig. 3d, alter-SIPE displays a single peak situated at about 2.5 Å of the distance between adjacent Li^+ – Li^+ centres, while additional peaks ranging from 4 to 9 Å (grey circles) were observed for random-, block- and homo-SIPEs. Combined with the lowest Li–Li coordination number in alter-SIPE (Supplementary Fig. 4), Li distribution in alter-SIPE could be more homogeneous and less aggregated than that in other SIPEs. These MD results are supported by Raman and ^7Li solid-state nuclear magnetic resonance (NMR) spectroscopies. Because the Raman S–N bending peak in Li-salt monomers is sensitive to cation–anion complexation^{37,38}, the maximal ratio of contact ion pair (CIP, 758 cm^{-1}) and aggregated ion cluster (AGG) in alter-SIPE (Supplementary Table 9) indicates reduced formation of aggregations via ionic interactions³⁹. On the other hand, the other three SIPEs show gradually more dominant presence of AGGs upshifted to 764 cm^{-1} (Fig. 3e). In NMR spectra, lithium nuclei in alter-SIPE were most shielded, with a negative shift (–0.58 ppm) among different sequences (Fig. 3f) because of enhanced coordination with adjacent ethers, consistent with the maximal percentage of Li–O (O atoms in C–O–C) coordination interaction as revealed by MD (Supplementary Figs. 7 and 8), illustrating a uniform Li^+ distribution environment and modulated Li^+ solvation structure. In contrast, lithium nuclei in random-, block- and homo-SIPEs were less shielded, with chemical shifts gradually changing to –0.17 ppm, suggesting impeded Li^+ dissociation from anionic centres.

Enhanced Li^+ dissociation in alter-SIPE is supported by the binding strength of ion pairs in different sequences using truncated chain models^{40,41} via density function theory (DFT) calculations. When ionic

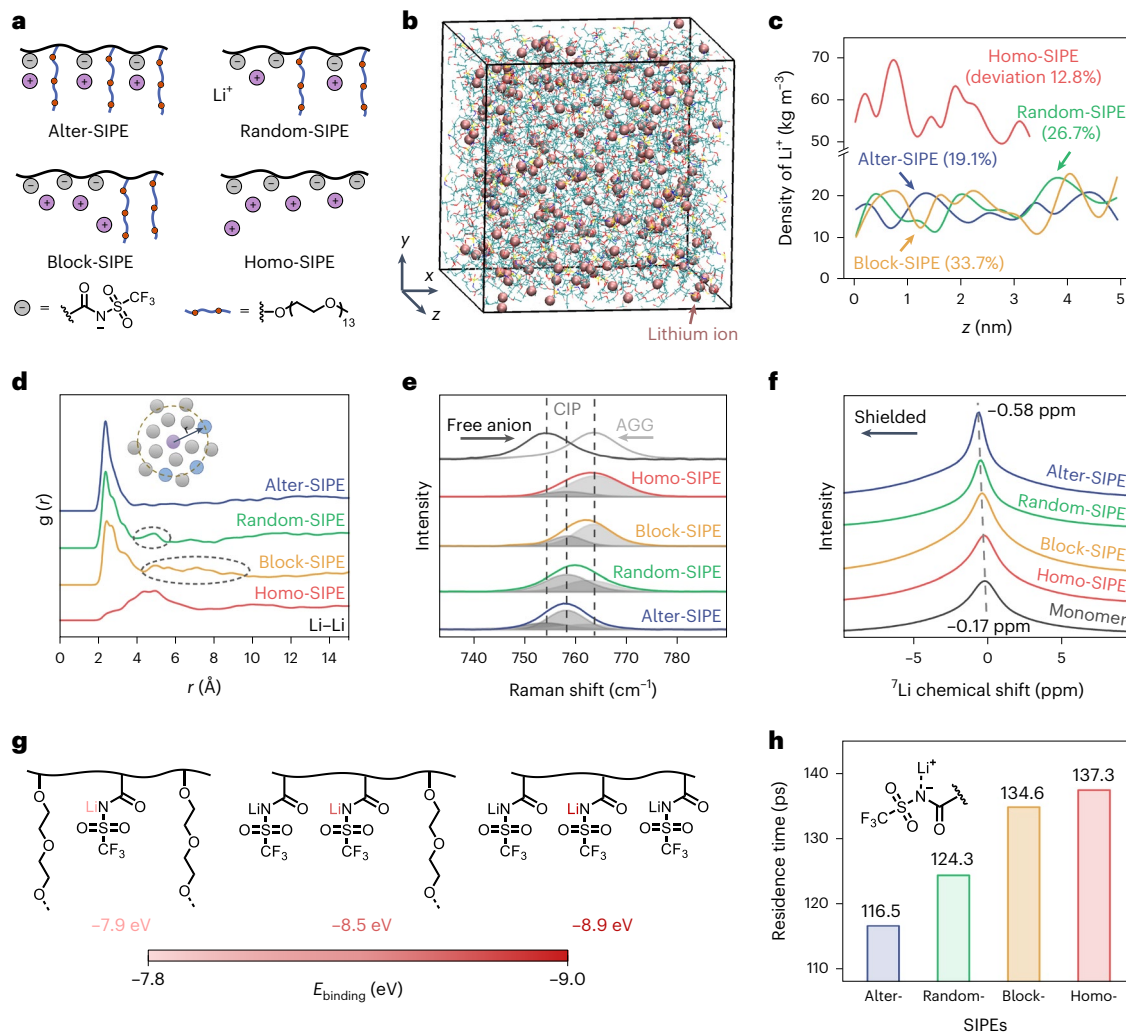


Fig. 3 | Analysis of Li^+ dissociation in different polymer sequences.

a, Illustration of alter-, random-, block- and homo-SIPEs. **b**, Snapshot of MD simulation for alter-SIPE at 30 °C. **c**, Li^+ density distribution and coefficients of s.d. along the z axis. **d**, RDF of Li–Li pairs. **e**, Raman spectra (**e**) and solid-state

^7Li NMR (**f**) of SIPEs. **g**, Structures and binding energy of alter-, random-/block- and homo-SIPE with truncated chain models by DFT calculation. **h**, Average residence times (τ) between Li^+ ions and anions. **g**(r) represents the radial distribution function and r is the distance of Li–Li pairs.

and PEO units were structured alternately, the dissociation of uniformly distributed Li^+ could be facilitated by coordination with adjacent O atoms from PEO units, which resulted in the minimal binding energy (E_{binding}) between Li^+ and polymer of -7.9 eV (Fig. 3g and Supplementary Figs. 10 and 11), where higher E_{binding} values of -8.5 and -8.9 eV were obtained for random-/block- and homo-SIPEs, respectively. This trend is consistent with that of the average residence time (τ) for Li^+ and anions, from 116.5 to 137.3 ps by MD, where alter-SIPE provides the shortest τ (Fig. 3h) owing to the fastest dissociation kinetics of Li^+ (ref. 39). These simulation and experimental results demonstrate the effective role of regulating the polymer sequence in promotion of Li^+ -anion dissociation.

Tailoring chain mobility and dissociation of alter-SIPEs

We tuned Li^+ dissociation and the segmental chain motion of polymer side chains to increase ion conduction in alter-SIPEs. Five alter-SIPEs (**P1**–**P5**; Fig. 4a and Supplementary Table 6), composed of the same vinyl ethers but different Li-salt monomers (**P1**, $\text{R}=\text{CF}_3$; **P2**, CH_3 ; **P3**, 4- CF_3 -Ph; **P4**, Ph; **P5**, 4- CH_3 O-Ph) were synthesized by photo-CRAP. Kinetic studies verified controlled chain growth and equal consumption of comonomers in five reactions, indicating an alternating

sequence (Supplementary Fig. 12). The Li-salt monomers of both **P1** and **P3** led to considerably higher dissociation constants (K_a) in solution ($K_a = 0.048, 0.052 \text{ mol l}^{-1}$) and in the polymer matrix at varying concentration (Fig. 4b and Supplementary Figs. 13 and 14)⁴², which are higher than those in **P2**, **P4** and **P5** with non-fluorinated groups, suggesting that trifluoromethyl substituents promote dissociation owing to their electron-withdrawal effect. Meanwhile, **P1** and **P2** with alkyl substituents have lower T_g (2 and 8 °C, respectively; Fig. 4c and Supplementary Fig. 15) than **P3**–**P5** with aromatic groups, supporting the premise that higher chain mobility is realized by structural modulation. Among five alter-SIPEs, **P1** yielded the best ion conductivity due to its high dissociation and chain mobility, which leads us to maintain trifluoromethyl in following structural optimization.

We then examined different lengths of PEO-based monomer by varying the repeating number (n) of ethylene oxide to further improve ionic conduction. Five alter-SIPEs ($n = 5, 8, 13, 17$ and 23 for **P6**–**P10**, respectively; Fig. 4d) were synthesized by copolymerization, and their molecular weights as measured by ^{19}F NMR ($M_{n,\text{NMR}}$), were close to expected values ($M_{n,\text{calc}}$; Fig. 4e and Supplementary Fig. 16). As n was increased from 2 to 13 (**P1** and **P6**–**P8**), T_g decreased from 8 to -32 °C where σ scaled up with declining T_g , yielding $4.2 \times 10^{-5} \text{ S cm}^{-1}$ for **P8** (Fig. 4f). Continued increments of n from 13 to 23 (**P8**–**P10**)

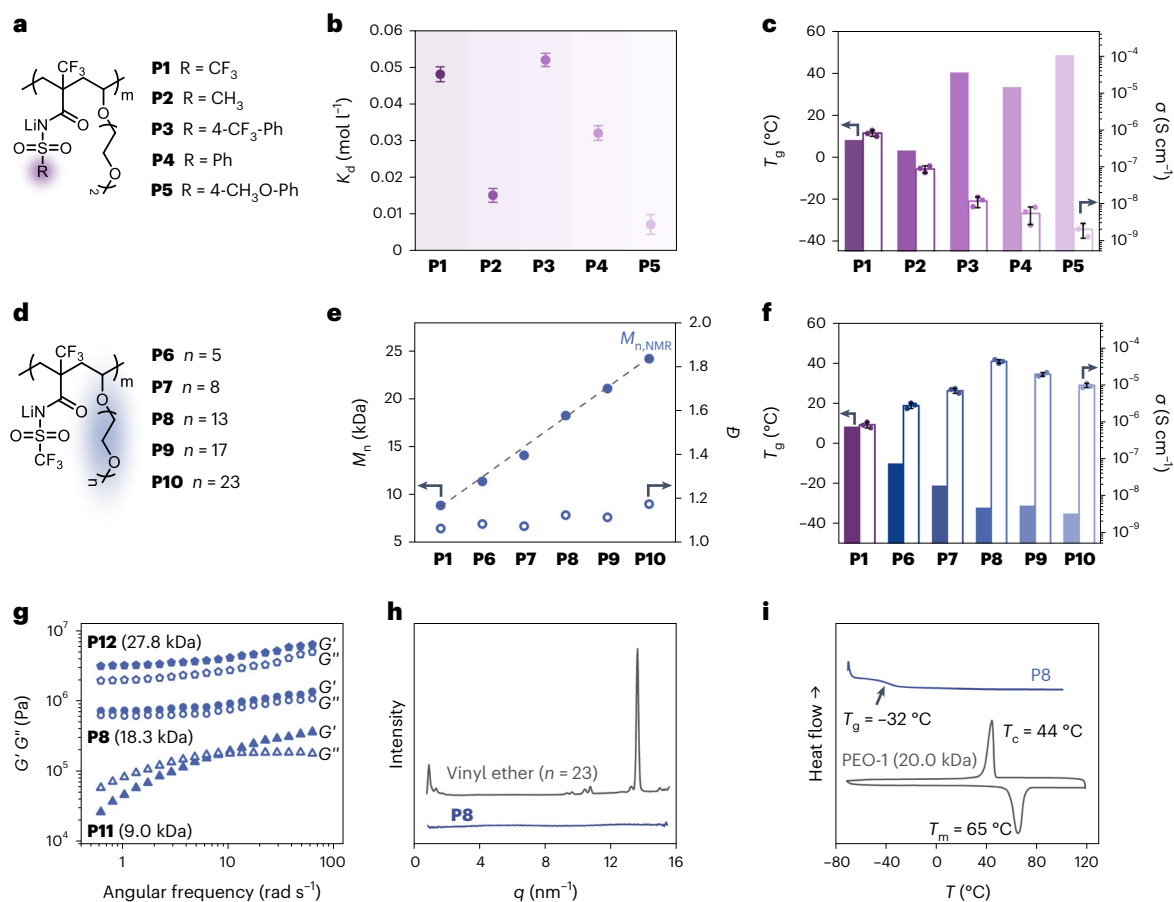


Fig. 4 | Tailoring polymer structures and characterizations of thermal, Li⁺ transport and mechanical properties. **a**, Structures of alter-SIPE (**P1**–**P5**, $m = 20$) with varying R groups. **b**, Ionic dissociation constants of lithium salt monomers in **P1**–**P5**. **c**, σ (30 °C) and T_g of **P1**–**P5**. **d**, Structures of **P6**–**P10** ($m = 20$) with varying length of PEO. **e**, $M_{n,calc}$ (dashed line), $M_{n,NMR}$ and molecular weight

distribution (\bar{D}) of alter-SIPEs. **f**, σ (30 °C) and T_g of alter-SIPEs. **b**, **c**, **f**, K_d and T_g values are mean \pm s.d. of three independent replicates. **g**, Mechanical property of alter-SIPEs with the same repeating units but different $M_{n,NMR}$. **h**, SAXS profiles of **P8** and the vinyl ether monomer with $n = 23$ in PEO. **i**, DSC curves of **P8** and PEO-1 ($M_n = 20.0$ kDa).

reduced σ to 9.6×10^{-6} S cm⁻¹, which can be attributed to reduction in Li⁺ concentration from 1.18 to 0.75 mol l⁻¹ in the polymer matrix (Supplementary Table 7) and in substantial changes in chain flexibility ($T_g = -32$ to -35 °C; Supplementary Fig. 17). Therefore, $n = 13$ in **P8** was maintained to provide maximal conductivity among **P1**–**P10**. We synthesized **P11** and **P12** with the same repeating units as **P8** but different $M_{n,NMR}$ (9.0 and 27.8 kDa; Supplementary Fig. 18) to probe the influence of molecular weight. As analysed by rheological studies (Fig. 4g), **P8** and **P12** retained higher storage moduli (G') than loss moduli (G''), evidencing a viscoelastic solid feature where **P11** provides $G' < G''$ at low frequencies, suggesting a viscoelastic liquid state. Although the stronger mechanical strength of **P8** and **P12** compared with that of **P11** could be favourable for lithium dendrite suppression⁴³, **P12** yielded reduced σ (1.2×10^{-5} S cm⁻¹; Supplementary Table 8) relative to **P8** due to constrained chain mobility.

Chain mobility was not restricted by the crystallization of PEO pendants in **P8**. When small-angle X-ray scattering (SAXS) was conducted with **P8**, no discernible sharp peak was found at ambient temperature (Fig. 4h), suggesting that PEO crystallization is suppressed by alternative insertion of ionic intervals. The amorphous property shows good agreement with the absence of T_m in **P8** (Fig. 4i), where PEO-1 of an analogous molecular weight (20.0 kDa) to **P8** exhibits peaks of crystallization and melting ($T_c = 44$ °C, $T_m = 65$ °C). The amorphous microstructure of alter-SIPE is beneficial for chain movement, and could avoid abrupt reduction in ion transport caused by crystallization.

Sequence-assisted ion transport and Li⁺ conduction

Alter-SIPE **P8** attained the highest ionic conductivity of 4.2×10^{-5} S cm⁻¹ at 30 °C and 1.7×10^{-4} S cm⁻¹ at 70 °C, which is outstanding for SPEs provided with the largely immobilized anionic moieties. The ionic conductivity of **P8** was between one and three orders of magnitude higher than random- and block-SIPEs (Fig. 5a), regardless of its comparable or reduced chain motion (Supplementary Fig. 19), confirming the essential role of sequence control on ion transport beyond T_g . Moreover, when PEO-1 was examined with lithium bis(trifluoromethylsulfonyl)imide (LiTFSI) as a dual-ion SPE, it crystallized at 30 °C and exhibited one-tenth of the bulk conductivity of **P8**. Based on Vogel–Tammann–Fulcher plots of conductivities measured at varying temperature (Fig. 5b and Supplementary Equation (9)), **P8** exhibited the lowest pseudo-activation energy (B parameter, 4.8 kJ mol⁻¹) among the four SIPEs (Supplementary Table 10), showing an effectively reduced mass transport barrier assisted by sequence control. We evaluated σ_{Li^+} to partition effective Li⁺ transport from overall ionic conductivity. Alter-SIPE **P8** yielded high σ_{Li^+} (0.84–0.93) between 30 and 70 °C based on the Bruce–Vincent method⁴⁴, showing stable single-ion conduction characteristics (Fig. 5c and Supplementary Table 11). Of note is that **P8** yielded $\sigma_{Li^+} = 3.9 \times 10^{-5}$ S cm⁻¹ while the dual-ion SPE of PEO-1 provided only 1.8% Li⁺ conduction ($\sigma_{Li^+} = 7.1 \times 10^{-7}$ S cm⁻¹) for **P8** due to its low σ_{Li^+} (0.21). For random-, block- and homo-sequences ($\sigma_{Li^+} = 0.90$ –0.95), the lower σ_{Li^+} values are mainly due to much weaker dissociation tendency, with no apparent correlation to crystallization (Supplementary Fig. 20).

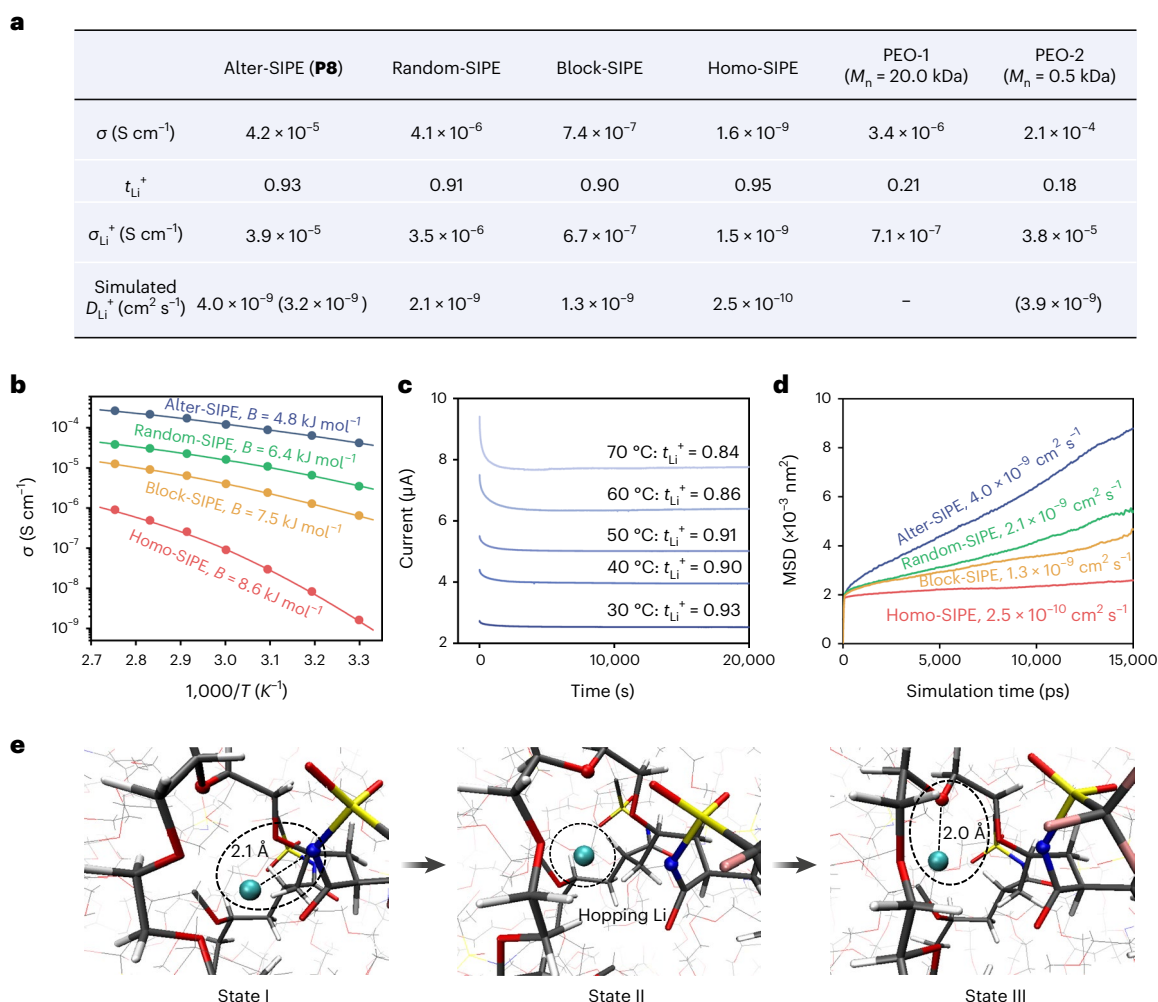


Fig. 5 | Investigation of transport pathway and Li⁺ conduction. **a**, Summarized results of t_{Li}^+ , ionic conductivity, Li⁺ conductivity and simulated Li⁺ diffusion coefficient (experimental values in parentheses) at 30 °C. LiTFSI was blended with PEO-1 and PEO-2 at a Li:O ratio of 1:15. **b**, Vogel–Tammann–Fulcher plots of

ionic conductivity for different SIPEs. **B** represents the pseudo-activation energy. **c**, Investigation of t_{Li}^+ with alter-SIPE at varying temperature. **d**, MSD of Li⁺ at 30 °C for different SIPEs. **e**, Screenshots of Li⁺ transport pathway in alter-SIPE by MD simulation. C, grey; H, white; O, red; N, blue; S, yellow; F, pink; Li, cyan.

The high Li⁺ mobility in **P8** was also supported by the narrow signal in ⁷Li NMR (Fig. 3f), agreeing with other highly conductive solid-state systems⁴⁵. Hence, alter-SIPE **P8** successfully delivered high Li⁺ conduction in a dry polymer system that is on a par with the liquid-like dual-ion electrolyte PEO-2 (Supplementary Table 12) measured at 30 °C.

As tracked by mean-squared displacement (MSD), the high Li⁺ conductivity of alter-SIPE **P8** was supported by a steeper slope of Li⁺ diffusion coefficient ($D_{Li}^+ = 4.0 \times 10^{-9}$ cm² s⁻¹) at 30 °C, surpassing random-, block- and homo-sequences (Fig. 5d). Consistent with the simulated D_{Li}^+ of **P8**, experimental D_{Li}^+ as measured by pulsed-field gradient solid-state NMR was equivalent to that of liquid-like PEO-2 electrolyte ($D_{Li}^+ = 3.2 \times 10^{-9}$ versus 3.9×10^{-9} cm² s⁻¹). This diffusion coefficient is comparable to a highly conductive zwitterion electrolyte³² and a liquid crystal–ionic liquid polymer composite system⁴⁵, indicating accelerated ion transport kinetics in alter-SIPE compared with the other three sequences. To visualize the Li⁺ transport pathway, chronological screenshots showing the movement of a specific Li atom in alter-SIPE were collected by MD simulation (Fig. 5e). Initially Li⁺ is mainly coordinated with the anchoring anionic site with L–N distance 2.1 Å (state I). Subsequently Li⁺ undergoes an intermediate state II in which Li⁺ partially dissociates from the N centre of an anion and hops to the adjacent PEO pendant. In the third step, Li⁺ migrates along the alternating structure and forms Li–O coordination, resulting in a Li–O

distance of 2.0 Å (state III). It is also possible for Li⁺ to hop back to another anionic centre and return to state I (Supplementary Fig. 5), revealing a contiguous avenue for ion migration⁴⁶. Collectively, the proximity between alternately arranged polyanions and PEO anchoring groups could induce concerted PEO–Li⁺–anion migration and a unique sequence-assisted structural transport pathway. The competitive ligand coordination and coulombic interactions from the lithium salt and PEO pendant, rather than counteracting each other, work in synergy and induce ‘site-to-site’ continuous transport.

Enabling ASSBs at ambient temperature

Symmetric Li||Li cells were assembled to explore the cycling stability of different sequences in SIPEs. Random-, block- and homo-SIPEs failed to start cell operation at 30 °C because of markedly lower conductivity. Blending random- and block-SIPEs with 20 wt% PEO-2 increased conductivity comparable to that of **P8** at 30 °C (Supplementary Table 13), which facilitated Li plating-stripping cycling for 600 and 900 cycles with exacerbating polarization during cycling, indicating an unstable flux of Li⁺. When the liquid electrolyte of the PEO-2–LiTFSI composite was examined, dendritic lithium (Supplementary Fig. 24) formed and shorted the cell within 400 h. By contrast, **P8** displayed stable cycling for >1,500 h at 0.05 mA cm⁻²_{geo} (current density per geometric area of electrode; Fig. 6a and Supplementary Fig. 25) due to

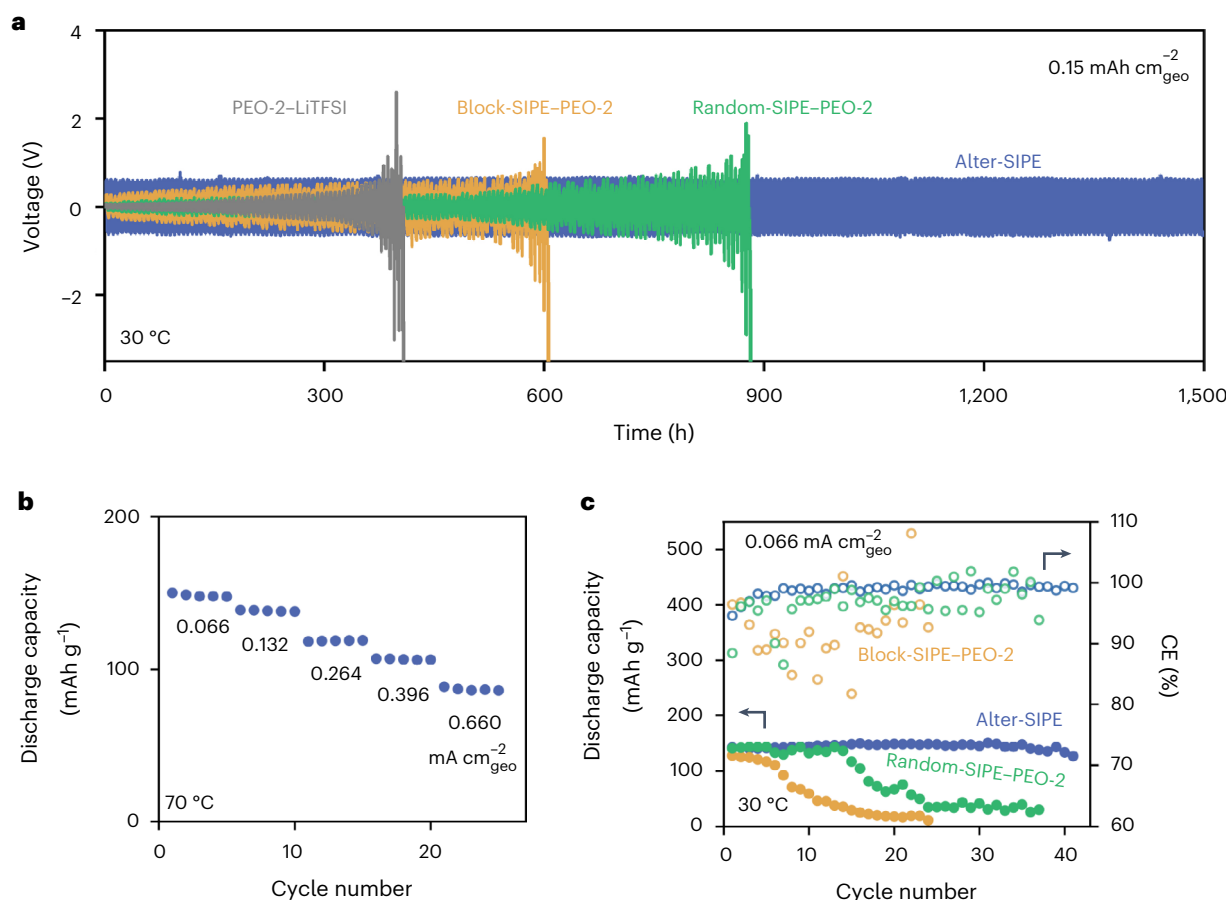


Fig. 6 | Dendrite-suppression behaviour and battery performance from ambient to elevated temperatures. a, Li plating-stripping test of Li||Li symmetric lithium cells with SIPEs at 0.05 mA cm⁻²_{geo} and 0.15 mA cm⁻²_{geo} (30 °C, polymer electrolyte thickness 150 μm). **b,** Reversibility of

charge–discharge at varying temperature and current for alter-SIPE **P8**. **c,** Galvanostatic cycling in Li||LFP cells at 30 °C. **a,c,** Electrolytes include **P8**, random-SIPE-PEO-2 (80:20 wt%), block-SIPE-PEO-2 (80:20 wt%) and LiTFSI-PEO-2 (Li:O = 1:20).

homogenized ion distribution and enhanced mechanical strength and electrochemical stability.

Facilitated by the high ion conduction of **P8** with minimized transport polarization, we present Li||**P8**||LiFePO₄ (LFP) ASSBs that enable stable cycling and high Coulombic efficiency (CE), at current densities of 0.066–0.660 mA cm⁻²_{geo} and operating temperatures of 30–70 °C and with a mass loading of 8.8 mg cm⁻²_{geo} for the LFP cathode. When cycled at 70 °C, high specific capacities of 148 and 139 mAh g⁻¹ were observed at 0.066 and 0.132 mA cm⁻²_{geo} (0.05 and 0.10 charge/discharge (C) rates, respectively; Fig. 6b and Supplementary Fig. 26). The use of 0.66 mA cm⁻²_{geo} (0.5 C) yielded a capacity of 86 mAh g⁻¹, comparable to PEO-based composite electrolytes at 60 °C^{47,48}. Promisingly, **P8** provides a high discharge capacity of 147 mAh g⁻¹ (Fig. 6c) and stable charge–discharge plateaus between 2.5–3.8 V at 30 °C (Supplementary Fig. 27). Note that electrode composition and processing have not been optimized, the high porosity of the LFP electrodes (Supplementary Table 14) indicates tortuosity in the electrode. Therefore, a current density of 0.066 mA cm⁻²_{geo} (0.05 C) was attempted for charge–discharge cycling at 30 °C. A high average CE of 99.3% was obtained with >40 cycles and 92% capacity retention at 30 °C. Comparatively, both random-SIPE-PEO-2 and block-SIPE-PEO-2 composites exhibited fluctuating CE and rapid capacity decay after 10–15 cycles, in accordance with accelerated dendrite formation during Li electrodeposition (Supplementary Fig. 28). The high discharge capacity and cycling stability⁴⁹ of alter-SIPE represent unprecedented improvement in dry SPE at ambient temperature (Supplementary Table 15), and our sequence-controlled method

demonstrates a promising strategy for effective promotion of ion conduction and enabling ASSB operation.

In summary, we have identified the fundamental impact of sequence control on Li⁺ dissociation and conduction, which endows desirable chain mobility and overcomes the inherent limitation of ion transport for solid-state polymer electrolytes. The alternating sequence of fluorinated Li-salt and PEO pendants enhances molecular-level homogeneity of ion distributions, modulated anion-Li⁺ complexation and hence improved Li⁺ dissociation and a unique sequence-assisted PEO-Li⁺-anion migration. In addition, alternating SIPE is able to demonstrate all-solid-state lithium metal battery operation at ambient temperature, addressing the long-standing problem with solid-state electrolytes. This work shows that polymer sequence can be more delicately programmed and various functionalities could be engineered, opening new avenues for highly efficient ion transport and versatile ion-conductive materials in energy devices beyond lithium batteries.

Online content

Any methods, additional references, Nature Portfolio reporting summaries, source data, extended data, supplementary information, acknowledgements, peer review information; details of author contributions and competing interests; and statements of data and code availability are available at <https://doi.org/10.1038/s41563-023-01693-z>.

References

1. Armand, M. & Tarascon, J. M. Building better batteries. *Nature* **451**, 652–657 (2008).

2. Albertus, P. et al. Challenges for and pathways toward Li-metal-based all-solid-state batteries. *ACS Energy Lett.* **6**, 1399–1404 (2021).
3. Li, M., Lu, J., Chen, Z. & Amine, K. 30 Years of lithium-ion batteries. *Adv. Mater.* **30**, 1800561 (2018).
4. Meng, Y. S., Srinivasan, V. & Xu, K. Designing better electrolytes. *Science* **378**, 1065 (2022).
5. Hobold, G. M. et al. Moving beyond 99.9% Coulombic efficiency for lithium anodes in liquid electrolytes. *Nat. Energy* **6**, 951–960 (2021).
6. Zhao, Q., Stalin, S., Zhao, C. Z. & Archer, L. A. Designing solid-state electrolytes for safe, energy-dense batteries. *Nat. Rev. Mater.* **5**, 229–252 (2020).
7. Banerjee, A., Wang, X., Fang, C., Wu, E. A. & Meng, Y. S. Interfaces and interphases in all-solid-state batteries with inorganic solid electrolytes. *Chem. Rev.* **120**, 6878–6933 (2020).
8. Chen, R. S., Li, Q. H., Yu, X. Q., Chen, L. Q. & Li, H. Approaching practically accessible solid-state batteries: stability issues related to solid electrolytes and interfaces. *Chem. Rev.* **120**, 6820–6877 (2020).
9. Lopez, J., Mackanic, D. G., Cui, Y. & Bao, Z. N. Designing polymers for advanced battery chemistries. *Nat. Rev. Mater.* **4**, 312–330 (2019).
10. Li, Z. Y., Zhang, H. R., Sun, X. L. & Yang, Y. Mitigating interfacial instability in polymer electrolyte-based solid-state lithium metal batteries with 4 V cathodes. *ACS Energy Lett.* **5**, 3244–3253 (2020).
11. Xu, K. Nonaqueous liquid electrolytes for lithium-based rechargeable batteries. *Chem. Rev.* **104**, 4303–4418 (2004).
12. Bachman, J. C. et al. Inorganic solid-state electrolytes for lithium batteries: mechanisms and properties governing ion conduction. *Chem. Rev.* **116**, 140–162 (2016).
13. Bouchet, R. et al. Single-ion BAB triblock copolymers as highly efficient electrolytes for lithium-metal batteries. *Nat. Mater.* **12**, 452–457 (2013).
14. Wang, X. et al. Ultra-stable all-solid-state sodium metal batteries enabled by perfluoropolyether-based electrolytes. *Nat. Mater.* **21**, 1057–1065 (2022).
15. Ratner, M. A. & Shriver, D. F. Ion transport in solvent-free polymers. *Chem. Rev.* **88**, 109–124 (1988).
16. Bocharova, V. & Sokolov, A. P. Perspectives for polymer electrolytes: a view from fundamentals of ionic conductivity. *Macromolecules* **53**, 4141–4157 (2020).
17. Cheng, X. L., Pan, J., Zhao, Y., Liao, M. & Peng, H. S. Gel polymer electrolytes for electrochemical energy storage. *Adv. Energy Mater.* **8**, 1702184 (2018).
18. Mindemark, J., Lacey, M. J., Bowden, T. & Brandell, D. Beyond PEO-alternative host materials for Li⁺-conducting solid polymer electrolytes. *Prog. Polym. Sci.* **81**, 114–143 (2018).
19. Wang, J. R., Li, S. Q., Zhao, Q., Song, C. & Xue, Z. G. Structure code for advanced polymer electrolyte in lithium-ion batteries. *Adv. Funct. Mater.* **31**, 2008208 (2020).
20. Qiao, B. et al. Supramolecular regulation of anions enhances conductivity and transference number of lithium in liquid electrolytes. *J. Am. Chem. Soc.* **140**, 10932–10936 (2018).
21. Ma, Q. et al. Single lithium-ion conducting polymer electrolytes based on a super-delocalized polyanion. *Angew. Chem. Inter. Ed. Engl.* **55**, 2521–2525 (2016).
22. Li, J. H. et al. Polymers in lithium-ion and lithium metal batteries. *Adv. Energy Mater.* **11**, 2003239 (2021).
23. Zhang, H. et al. Single lithium-ion conducting solid polymer electrolytes: advances and perspectives. *Chem. Soc. Rev.* **46**, 797–815 (2017).
24. Lu, Y. Y., Korf, K., Kambe, Y., Tu, Z. Y. & Archer, L. A. Ionic-liquid-nanoparticle hybrid electrolytes: applications in lithium metal batteries. *Angew. Chem. Inter. Ed. Engl.* **53**, 488–492 (2014).
25. Doyle, M., Fuller, T. F. & Newman, J. The importance of the lithium ion transference number in lithium polymer cells. *Electrochim. Acta* **39**, 2073–2081 (1994).
26. Li, S. P. et al. Single-ion homopolymer electrolytes with high transference number prepared by click chemistry and photoinduced metal-free atom-transfer radical polymerization. *ACS Energy Lett.* **3**, 20–27 (2018).
27. Jangu, C. et al. Sulfonimide-containing triblock copolymers for improved conductivity and mechanical performance. *Macromolecules* **48**, 4520–4528 (2015).
28. Lutz, J. F., Ouchi, M., Liu, D. R. & Sawamoto, M. Sequence-controlled polymers. *Science* **341**, 1238149 (2013).
29. Barnes, J. C. et al. Iterative exponential growth of stereo- and sequence-controlled polymers. *Nat. Chem.* **7**, 810–815 (2015).
30. Trigg, E. B. et al. Self-assembled highly ordered acid layers in precisely sulfonated polyethylene produce efficient proton transport. *Nat. Mater.* **17**, 725–731 (2018).
31. Mao, G., Saboungi, M.-L., Price, D. L., Armand, M. B. & Howells, W. S. Structure of liquid PEO-LiTFSI electrolyte. *Phys. Rev. Lett.* **84**, 5536–5539 (2000).
32. Makhlooghiazad, F. et al. Zwitterionic materials with disorder and plasticity and their application as non-volatile solid or liquid electrolytes. *Nat. Mater.* **21**, 228–236 (2022).
33. Cowie, J. M. G. *Alternating Copolymers* (Plenum Press, 1985).
34. Corrigan, N. et al. Reversible-deactivation radical polymerization (controlled/living radical polymerization): from discovery to materials design and applications. *Prog. Polym. Sci.* **111**, 101311 (2020).
35. Zhao, Y. et al. Controlled radical copolymerization of fluoro-alkenes by using light-driven redox-relay catalysis. *Nat. Synth.* **2**, 653–662 (2023).
36. Zhang, W. X. et al. Molecularly tunable polyanions for single-ion conductors and poly(solvate ionic liquids). *Chem. Mater.* **33**, 524–534 (2021).
37. Atik, J. et al. Cation-assisted lithium-ion transport for high-performance PEO-based ternary solid polymer electrolytes. *Angew. Chem. Inter. Ed. Engl.* **60**, 11919–11927 (2021).
38. Ma, M. Y. et al. Designing weakly solvating solid main-chain fluoropolymer electrolytes: synergistically enhancing stability toward Li anodes and high-voltage cathodes. *ACS Energy Lett.* **6**, 4255–4264 (2021).
39. Nurnberg, P. et al. Superionicity in ionic-liquid-based electrolytes induced by positive ion-ion correlations. *J. Am. Chem. Soc.* **144**, 4657–4666 (2022).
40. Huang, Y. F. et al. A relaxor ferroelectric polymer with an ultrahigh dielectric constant largely promotes the dissociation of lithium salts to achieve high ionic conductivity. *Energy Environ. Sci.* **14**, 6021–6029 (2021).
41. Chen, F., Wang, X., Armand, M. & Forsyth, M. Cationic polymer-in-salt electrolytes for fast metal ion conduction and solid-state battery applications. *Nat. Mater.* **21**, 1175–1182 (2022).
42. Ue, M. & Mori, S. Mobility and ionic association of lithium salts in a propylene carbonate-ethyl methyl carbonate mixed solvent. *J. Electrochem. Soc.* **142**, 2577–2581 (1995).
43. Khurana, R., Schaefer, J. L., Archer, L. A. & Coates, G. W. Suppression of lithium dendrite growth using cross-linked polyethylene/poly(ethylene oxide) electrolytes: a new approach for practical lithium-metal polymer batteries. *J. Am. Chem. Soc.* **136**, 7395–7402 (2014).
44. Bruce, P. G. & Vincent, C. A. Steady state current flow in solid binary electrolyte cells. *J. Electroanal. Chem.* **225**, 1–17 (1987).
45. Wang, Y. et al. Solid-state rigid-rod polymer composite electrolytes with nanocrystalline lithium ion pathways. *Nat. Mater.* **20**, 1255–1263 (2021).

46. Yu, Z. et al. A dynamic, electrolyte-blocking, and single-ion-conductive network for stable lithium-metal anodes. *Joule* **3**, 2761–2776 (2019).
47. Zhang, X. K. et al. Vertically aligned and continuous nanoscale ceramic-polymer interfaces in composite solid polymer electrolytes for enhanced ionic conductivity. *Nano Lett.* **18**, 3829–3838 (2018).
48. Qing, X. et al. A functionalized metal organic framework-laden nanoporous polymer electrolyte for exceptionally stable lithium electrodeposition. *Chem. Commun.* **56**, 15533–15536 (2020).
49. Lu, J. et al. The role of nanotechnology in the development of battery materials for electric vehicles. *Nat. Nanotechnol.* **11**, 1031–1038 (2016).

Publisher's note Springer Nature remains neutral with regard to jurisdictional claims in published maps and institutional affiliations.

Springer Nature or its licensor (e.g. a society or other partner) holds exclusive rights to this article under a publishing agreement with the author(s) or other rightsholder(s); author self-archiving of the accepted manuscript version of this article is solely governed by the terms of such publishing agreement and applicable law.

© The Author(s), under exclusive licence to Springer Nature Limited 2023

Methods

Synthesis of P1–P12

An oven-dried 5 ml vial equipped with a stir bar was charged with lithium salt monomer (LSM), poly(ethylene glycol) methyl ether (PEO_n-VE), chain transfer agent (CTA), photocatalyst (PC), synthesized according to ref. 50 ([LSM] = 1.0 mmol, [LSM]:[PEO_n-VE]:[CTA]:[PC] = 20:20:1:0.02 for **P1–P10**, [LSM]:[PEO_n-VE]:[CTA]:[PC] = 10:10:1:0.02 for **P11**, [LSM]:[PEO_n-VE]:[CTA]:[PC] = 30:30:1:0.02 for **P12**) and 2 ml of DMSO. After sealing the vial with a rubber septum, the solution was deoxygenated with three freeze–pump–thaw cycles under N₂. The mixture was then placed in front of a 13 W white light-emitting diode bulb for 24 h while cooling with compressed air to maintain 25 °C. After the reaction, an internal standard (ethyl benzoate, 1.0 mmol) was added to the mixture with stirring. A small aliquot was taken and analysed by ¹H NMR to yield monomer conversion (conversion(%)). The sample was precipitated with toluene three times then dried under vacuum at 70 °C for 12 h before characterization.

For details of materials used, see section 1 in Supplementary Information.

For the synthesis of alter-, random-, block- and homo-SIPs, see section 2.2 in Supplementary Information.

For the synthesis and characterization of LSMs, PEO_n-VEs and CTAs, see sections 6.1–6.3 in Supplementary Information.

Materials characterization

NMR spectroscopy. Nucleic magnetic resonance measurements were conducted on an Advance III 400 MHz Bruker instrument at 25 °C. Chemical shifts were measured according to the signal of either residual chloroform (7.26 ppm) in CDCl₃ or residual dimethyl sulfoxide (2.50 ppm) in dimethyl sulfoxide-*d*₆ and are reported in δ units (ppm). For solid-state NMR, a Bruker Advance III 400 MHz instrument was equipped with a static high-power probe to ensure a wide spectral excitation bandwidth by short, high-power excitation pulses⁷. Li NMR spectra were collected using an acquisition time of 0.0198 s, relaxation delay of 10 s, prescan delay of 10 μ s and 128 scans. Pulsed-field gradient solid-state NMR measurements were carried out using an Advance III 600 MHz Bruker instrument and Diff50 probe at 30 °C. Solid polymer samples were packed into 5 mm Schott E NMR tubes and sealed with Teflon tape. Sixty-four scans at each gradient strength were used to ensure a good signal:noise ratio. Gradient pulse duration δ = 1 ms with a diffusion time Δ of 25 ms were used to obtain diffusion coefficients.

Size exclusion chromatography. Size exclusion chromatography measurements were performed on a TOSOH instrument (0.1 M LiBr in *N,N*-dimethylformamide) equipped with a Bryce refractive index detector, and were conducted at 50 °C at an elution rate of 1 ml min⁻¹. Calibrations were performed with poly(methyl methacrylate) standards.

Rheology measurements. Rheology studies were conducted using a HAAKE MARS III rheometer with a 20 mm parallel plate in a convection oven. Oscillatory shear experiments were carried out at controlled strain amplitude γ = 1% within the angular frequency range ω = 0.1–60 rad s⁻¹ at room temperature. Samples were dried under vacuum at 60 °C for 24 h before measurement.

SAXS. SAXS was conducted using a Pilatus3R 200K-A detector monochromatic X-ray source (Xenocs2.0) with 8KeV Cu K α radiation (wavelength λ = 0.15406 nm and sample–detector distance 300 mm). The two-dimensional scattering patterns were azimuthally integrated into one-dimensional plots of scattering intensity versus scattering vector q , where $q = 4\pi \sin\theta/\lambda$ and scattering angle was 2θ . The samples were dried under vacuum at 60 °C for 24 h and SAXS was measured under vacuum at room temperature.

Raman spectroscopy. Raman measurements were obtained on a HORIBA JobinYvon Raman spectrophotometer (XploRA) with an excitation laser of 785 nm wavelength at room temperature.

Electrochemical measurements

Electrochemical impedance spectroscopy. Electrochemical impedance spectroscopy measurements were performed on an electrochemical analyser and workstation (Bio-logic VMP-300 and CHI 760E). Polymer electrolytes (PE) were heated to the desired temperatures for 1 h before measurements. Ionic conductivity (σ) was measured by alternative current impedance spectroscopy using a stainless steel/PE/stainless steel cell over a frequency range of 0.1–10⁶ Hz at 5 mV amplitude; σ was calculated based on the following equation:

$$\sigma = \frac{L}{RS}$$

where L is the thickness (0.15 mm) of the electrolyte, $R(\Omega)$ is the bulk resistance of the electrolyte measured by alternative current impedance spectroscopy and S is the contact area (0.28 cm²) between electrolyte and the stainless-steel.

Li|Li symmetrical-cell cycling. The Li plating-stripping test was monitored by the LAND cycle test system using a symmetric Li/PE/Li cell with a current density of 0.05 mA cm_{geo}⁻² to evaluate Li stripping/plating performance.

Li|LFP full-cell cycling. Galvanostatic cycling was performed with a Li/PE/LFP(LiFeO₄) cell under varying current rate over a voltage range of 2.5–3.8 V using the LAND cycle test system.

For details of assembly of batteries, see section 5.1 in Supplementary Information.

Computational experiments

MD simulations. Simulations were performed using GROMACS⁵¹ (v.2019.3) with the all-atom OPLS force field. Detailed methods are described in section 3.2 of Supplementary Information.

DFT calculations. All DFT calculations conducted in this study were carried out using the Gaussian 16 suite of programmes. Detailed methods are given in section 3.3 of Supplementary Information.

Data availability

Source data are provided with this paper. Additional data supporting the findings of this study are included in the Supplementary Information.

References

50. Zhao, Y. et al. Organocatalyzed photoredox polymerization from aromatic sulfonyl halides: facilitating graft from aromatic C–H bonds. *Macromolecules* **51**, 938–946 (2018).
51. Hess, B., Kutzner, C., van der Spoel, D. & Lindahl, E. GROMACS 4: algorithms for highly efficient, load-balanced, and scalable molecular simulation. *J. Chem. Theory Comput.* **4**, 435–447 (2008).

Acknowledgements

This research was financially supported by the National Natural Science Foundation of China (no. 21971044 to M.C. and 52003231 to X.L.), the Shanghai Pilot Program for Basic Research–Fudan University 21TQ1400100 (no. 21TQ007 to M.C.) and the State Key Laboratory of Molecular Engineering of Polymers and Duke Kunshan University. We thank J. A. Johnson for helpful discussions.

Author contributions

S.H., X.L. and M.C. conceived the idea and designed the experiments. S.H. conducted major experiments and prepared the draft article. S.H. and X.L. contributed molecular dynamic simulations. P.W. and Y.Z. contributed DFT calculations. S.H., H.W., Y.G. and L.Z. conducted

materials characterizations. S.H., Y.S.-H., X.L. and M.C. interpreted the data and completed the final manuscript writing.

Competing interests

The authors declare no competing interests.

Additional information

Supplementary information The online version contains supplementary material available at <https://doi.org/10.1038/s41563-023-01693-z>.

Correspondence and requests for materials should be addressed to Yang Shao-Horn, Xinrong Lin or Mao Chen.

Peer review information *Nature Materials* thanks Renaud Bouchet and the other, anonymous, reviewer(s) for their contribution to the peer review of this work.

Reprints and permissions information is available at www.nature.com/reprints.